HRTEM investigation of trilling todorokite and nano-phase Mn-oxides in manganese dendrites

Huifang Xu,[1,*] Tianhu Chen,[1,2] and Hiromi Konishi[1]

[1]Department of Geoscience, and Materials Science Program, University of Wisconsin, Madison, Wisconsin 53706, U.S.A.
[2]College of Resources and Environmental Engineering, Hefei University of Technology, Hefei 230009, P.R. China

Abstract

We characterized manganese dendrites on three different substrate rocks (rhyolite, clayey siltstone, and limestone) using high-resolution transmission electron microscopy. Manganese dendrites are mainly composed of nanometer scale Mn-(hydr)oxides, Fe-(oxy)hydroxide, sulfate, and clay minerals including hollandite, todorokite, birnessite, goethite, amorphous Fe-hydroxide, smectite, illite, and gypsum. Each sample has a different main manganese phase. Two dendrite samples have more than one manganese phase. Todorokite crystals on a limestone sample from Altmühl Valley, Germany, showed trilling intergrowths. Chain-width disorder and chain termination occur in todorokite. The sum of the numbers of octahedral wall layers and octahedral chains were equal at both sides beyond the termination. The chain termination rule was explained by the geometry of octahedral chains and the octahedral wall layer. The trilling intergrowths of todorokite might be formed by transforming the structure from birnessite to todorokite, or by multiple, epitaxial todorokite nucleations on octahedral wall layer of todorokite or birnessite. Based on chain-width disorder in the todorokite, we suggest that the todorokite might have been transformed from birnessite.

Keywords: Manganese dendrites, origin of the dendrites, microstructure, hollandite, todorokite, birnessite, Fe-hydroxide, transmission electron microscopy

Introduction

Manganese dendrites are black, hard, and pine branch-like, and they usually occur on the surfaces and microfractures of rocks. They are believed to be common products of terrestrial weathering processes and precipitation of aqueous manganese ions. Manganese dendrites and some desert vanish samples have been examined using X-ray powder diffraction, infrared spectroscopy, X-ray absorption spectroscopy, and electron microscopy (Krinsley 1998; Krinsley et al. 1995; McKeown and Post 2001; Nagy et al. 1991; Palmer et al. 1986; Perry and Adams 1978; Potter and Rossman 1977, 1979). The texture and growth mechanism of manganese dendrites were discussed using colloidal growth and fractal dimension theory (Chopard et al. 1991). Potter and Rossman (1979) systematically investigated the mineralogy of manganese dendrites, desert varnish, cave deposits, and stream deposits using infrared spectroscopy. They discovered Mn-oxide minerals hollandite, romanechite, and todorokite in manganese dendrites from different localities, but no pyrolusite contrary to what is stated in recent textbooks (Klein 2002; Wenk and Bulakh 2004). McKeown and Post (2001) characterized dendrites using X-ray absorption spectroscopy. Their results indicated that Mn-minerals in the dendrites, including birnessite-group minerals, had structural types of mixed tunnel, mixed layer, or both.

The detailed textures and the relationship among Mn-oxide phases and other minerals have not been well characterized. The main reasons for the difficulty of characterization include the extremely fine-grained polycrystalline structure of Mn-oxide and the similarity of X-ray powder diffraction patterns and infrared spectroscopy results among some manganese minerals (Post 1999; Potter and Rossman 1979). Other challenges include the presence of other mineral phases, e.g., clays, and the fact that the Mn-oxides typically occur as thin coatings. In this paper, we describe high-resolution transmission electron microscopy (HRTEM) observations of manganese dendrites from three localities and provide a more detailed look at the complex and varied Mn-oxide mineralogy in dendrites.

Samples and experimental methods

We examined three dendrite samples on three different substrate rocks. The first and second samples were taken from the mineral collections of the Department of Earth and Planetary Sciences, University of New Mexico. The first dendrite sample was collected from Deadwood, South Dakota. The dendrite identified as "pyrolusite dendrites" (UNM-M-987) occurred on an unweathered microfracture surface of a rhyolite. The second dendrite sample identified as "pyrolusite dendrites" (UNM-M-1054) occurred on a microfracture surface of clayey siltstone from an unknown locality. The third dendrite sample (AV1) is from the Altmühl Valley in Germany and was purchased from IKON Mining and Exploration. The dendrites occurred on the surface of limestone. The dendrites on rhyolite (UNM-M-987) and limestone (AV1) display a black color, whereas the dendrites on clayey siltstone (UNM-M-1054) display a brownish-black color (Fig. 1).

A JEOL JEM-2010 microscope equipped with an ISIS X-ray energy disper-
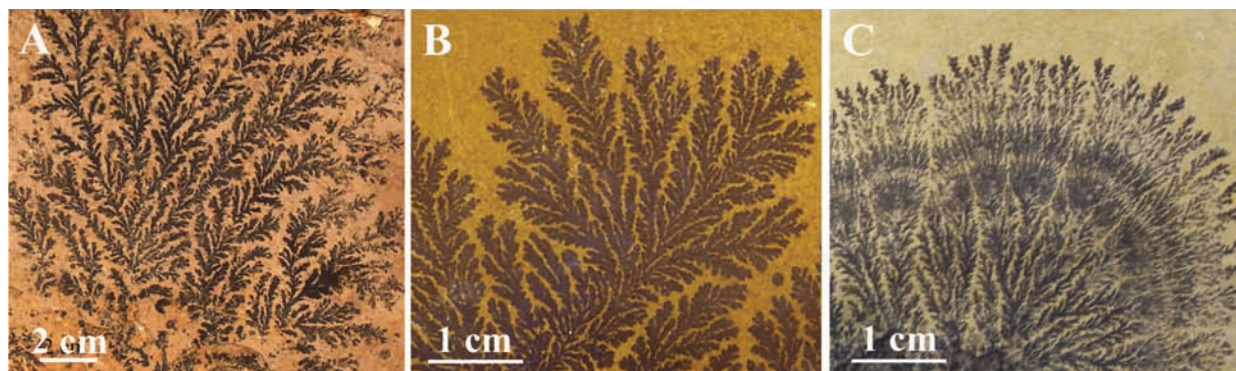
FIGURE 1. Hand specimen photos of the three manganese dendrites investigated. (**a**) On a fracture surface of a ryholite (UNM-M-987). (**b**) On a fracture surface of a clayey siltstone (UNM-M-1054). (**c**) On a fracture surface of a limestone from Altmühl Valley, Germany (AV1).

sive spectroscopy (EDS) system at the University of New Mexico was used for HRTEM, and operated at 200 keV. The chemical analysis was done using an EDS system with a Si (Li) detector. Experimentally measured k-factors for Na, K, Mg, Ni, and Mn (Xu and Wang 2000) and theoratical k-factors for Pb and Ba were used for quantitative analyses. A Philips CM200-UT microscope equipped with a Voyager X-ray EDS system at the Materials Science Center at the University of Wisconsin-Madison was also used for characterizing the dendrite sample (AV1) from Altmühl Valley, Germany, and operated at 200 keV. Quantitative analyses were carried out by using theoretical k-factors. The oxidation state of Mn is assumed to be +4, and all the results are normalized to 100%. Small amounts of dendrite for analysis were removed from specimens by gently scratching the dendrites with a tungsten needle under an optical microscope to minimize mineral contamination from their host rocks and were crushed between two glass slides with a few drops of ethanol. A drop of the resulting suspension was placed on a holey carbon film supported by a TEM Cu grid and air-dried without carbon coating.

RESULTS AND DISCUSSIONS

The manganese dendrites display a regular fractal pattern in hand specimens (Fig. 1) and are similar to other reported dendrites in text books (e.g., Klein 2002). The identification of mineral components and the characterization of the morphologies using scanning electron microscopy were difficult because of the colloidal texture and nanometer-scale sizes of minerals. Thus, both SEM and backscattered electron images did not show any detailed features even under low accelerating voltage image condition.

TEM results confirm early studies that dendrites from all our samples contain manganese minerals, but none of them contains pyrolusite. Selected-area electron diffraction patterns and X-ray energy dispersive spectra show that the dendrites from each locality had a different main manganese mineral. The first sample (UNM-M-987) contains more than one manganese phase. In the first sample, hollandite is the major phase (Fig. 2). The other phases are illite, gypsum, goethite, todorokite, and manganese–iron amorphous hydroxide. Figure 2g shows a low-magnification TEM image of fabric-like hollandite and todorokite thin layer. EDS analyses indicated that Ba and Pb were the main cations in the tunnels of hollandite and todorokite structures (Table 1). Some biological activity signatures of Ca-carbonate and amorphous silica-based porous frameworks were found in the manganese dendrite (Figs. 2e and 2h). Amorphous and nanoporous Fe-hydroxide (Fig. 2f) contains small amounts of P, S, and Cl, indicating involvement of biological activity in the Fe-hydroxide formation. Phosphorus could be a component of lipids released

from microbes. These findings may indicate that the formation of manganese dendrites involved microbial activity. It is suggested that the microbial activities were involved in formation desert vanish (Krinsley 1998; Krinsley et al. 1995).

In the second sample (UNM-M-987), the dendrites are composed of birnessite, spindle-like goethite, smectite, and illite (Fig. 3). Nanometer-size manganese oxides, birnessite with trace amount of hollandite, attach to illite and smectite and form aggregates in some areas (lower-right corner of Fig. 3a). Birnessite with sheet-like morphology is the main manganese mineral. The HRTEM image (inset in Fig. 3b) shows ~7 Å lattice fringes corresponding to (001) *d*-spacing of birnessite. The dendrites in the second sample have a relatively high Fe concentration compared with the dendrites in the first sample (UNM-M-987). Spindle-like goethite crystals cause a brownish color of the dendrites in the second sample.

Dendrites in the third sample (AV1) from Altmühl Valley, Germany, are composed of trilling intergrowths of todorokite, gypsum, illite, smectite, and iron-oxides (Figs. 4 and 5). Barium is the main cation in the tunnel positions of todorokite (Table 1). Individual platy fibers of todorokite are elongated along the **b*** direction. The trilling intergrowths were observed in todorokite fibers, which are twinned at 120° sharing their **c*** axes (Siegel and Turner 1983). The todorokite crystals also display octahedral chain width disorder (Fig. 5).

Barium, Pb, or both cations are concentrated in dendrites, where they may occupy todorokite and hollandite tunnels and birnessite interlayers. Results from the interaction between cryptomelane [$K(Mn^{2+},Mn^{4+})_8O_{16}$)] and Ba^{2+}- or Pb^{2+}-bearing solutions indicate that Ba and Pb prefer large tunnel positions in hollandite and todorokite structures (Feng et al. 1995; Tsuji and Komarneni 1993).

The clay minerals in the three manganese dendrites are similar to those obtained from desert rock varnish (Krinsley 1998; Krinsley et al. 1995). The dendrites are dominated by Mn- and Fe-oxide nano-phase minerals, whereas the desert vanish is dominated by clay minerals (Krinsley 1998; Krinsley et al. 1995). Desert rock varnish occurs on rock surfaces in a relatively dry environment. These fractures in which the investigated dendrites form are apparently of relatively high salinity and undersaturated with respect to water since water-soluble gypsum also occurs in
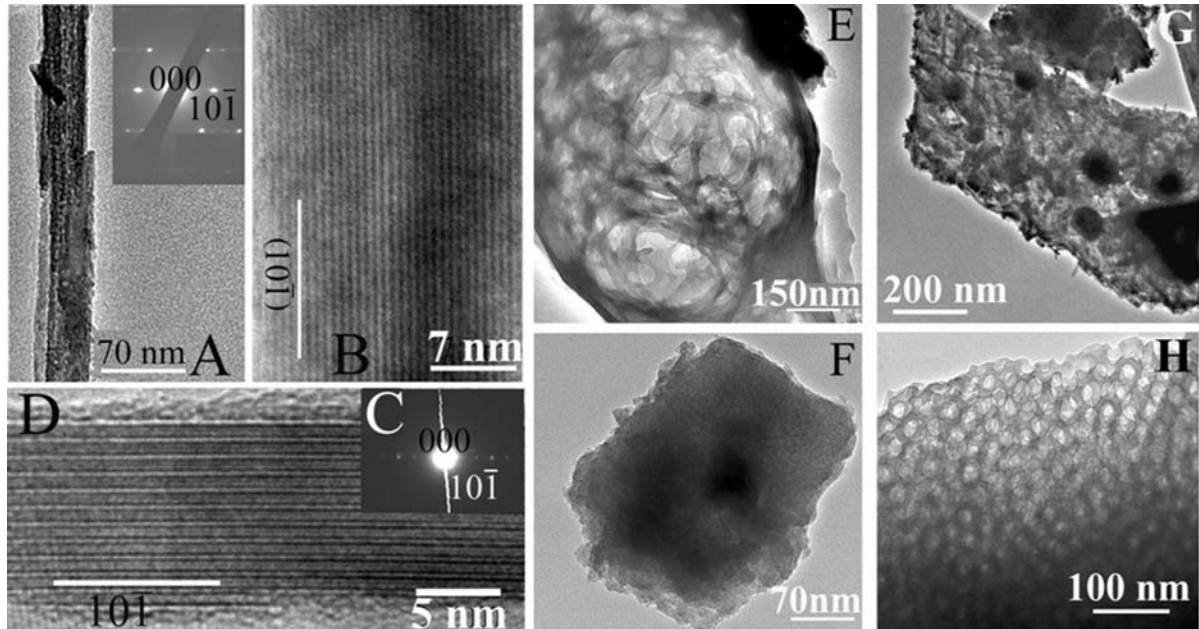
FIGURE 2. (**a**) Bright-field TEM image of a fiber-like hollandite crystal in the sample UNM-M-987 with a selected-area electron diffraction (SAED) pattern inserted at top-right corner. (**b**) High-resolution TEM image of the hollandite. (**c**) SAED pattern from the todorokite in **d**. (**d**) High-resolution TEM image of a todorokite crystal. (**e**) Bright-field TEM image of a Ca-rich microbial fragment showing porous and skeletal features. (**f**) TEM image of a P-bearing amorphous nano-porous Fe-hydroxide with worm-hole-like texture (see the sponge-like feature). (**g**) Bright-field TEM images show regular shape of a thin layer of fragment dominated by rod-like hollandite crystals from the sample UNM-M-987. (**h**) TEM bright-field image showing amorphous silica-based skeletal framework that is very similar to diatomaceous material.

the first and the third dendrite samples. Small amounts of water may be held in the microfractures even at water undersaturated condition due to the capillary effect as described by Kelvin's equation (Hiemenz and Rajagopalan 1997).

Todorokite can be formed from birnessite-like phylloman-ganate by removing every fourth octahedral chain from the birnessite octahedral sheet structure according to their structural difference. Where there is a fourth octahedral chain removed, a (001) octahedral wall layer of todorokite (an arrangement of triple octahedral chains) forms (Fig. 6). Although the construction of additional wall layers parallel to (100) is required for todorokite formation, nearly half of the todorokite structure is inherited from the original birnessite octahedral sheet structure. Because the birnessite octahedral sheet is characterized by pseudo-hexagonal symmetry, the resulting tunnel structure can

have three orientations, i.e., trilling intergrowth. The todorokite from sample AV1 might have been transformed from birnessite (Figs. 4b and 5). The morphology and the trilling intergrowths of the todorokite (Fig. 4b) resemble that of synthetic birnessite (Feng et al. 2004). The todorokite has chain-width errors that result in weak diffuse diffraction along a^* directions (Figs. 4c, 4d, and 5). The hollandite dominant nano-crystals with 120° rotational relationship also occur in the third dendrite sample (Fig. 7). This type of hollandite could be also transformed from precursor birnessite.

A topotactic relationship between todorokite and 10 Å verna-dite was observed before using HRTEM (Bodei et al. 2007), and it was suggested that todorokite formed from vernadite. Todorokite was also synthesized by autoclave treatment of birnessite (Golden et al. 1986, 1987), refluxing treatment of birnessite (Feng et al.

**TABLE 1.** Manganese mineral composition and formula normalized to 8 Mn

| Analysis no.	Mineral	MnO₂	BaO	PbO	Na₂O	K₂O	MgO	NiO	CaO	O	Mn	Ba	Pb	Na	K	Mg	Ca	Ni
M-987-02	hollandite	78.94	15.71	5.35		0				16	7.48	0.843	0.197		0			
M-987-03	hollandite	78.66	16.33	5.01		0				16	7.468	0.878	0.185		0			
M-987-08	hollandite	79.68	15.74	2.5		2.03				16	7.45	0.834	0.091		0.35			
M-987-12-1	hollandite	76.69	13.32	9.99		0				16	7.445	0.732	0.378		0			
M-987-12b	todorokite	72.43	18.56	9.01		0				12	5.471	0.794	0.265		0			
M-987-12	todorokite	70.8	20.67	8.53		0				12	5.424	0.897	0.255		0			
M-1054-15	birnessite	87.72		6.58		1.67	1.62	2.19	0.21	14	6.606		0.193		0.232	0.263	0.025	0.192
M-1054-16	birnessite	82.87		11.17		2.09	2.63		1.23	14	6.46		0.339		0.301	0.44	0.15	
M-1054-17	birnessite	81.82		11.19		2.17	4.03		0.79	14	6.367		0.339		0.312	0.676	0.095	
AV1-0612-01	todorokite	72.59	23.04		0.65	0.22	0.89	1.1	1.51	12	5.283	0.95		0.133	0.03	0.14	0.17	0.093
AV1-0612-02	todorokite	72.67	22.36		1.19	0.18	0.86	1.41	1.33	12	5.272	0.919		0.242	0.024	0.135	0.15	0.119
AV1-0612-04	todorokite	71.08	23.21		0.58	0.53	0.84	1.27	2.49	12	5.209	0.963		0.119	0.072	0.133	0.283	0.108

Notes: All the EDX analyses are normalized to 100 wt%. The analysis error is generally less than 4% for major elements (Mn in here) and about 10% or even larger for the minor elements.
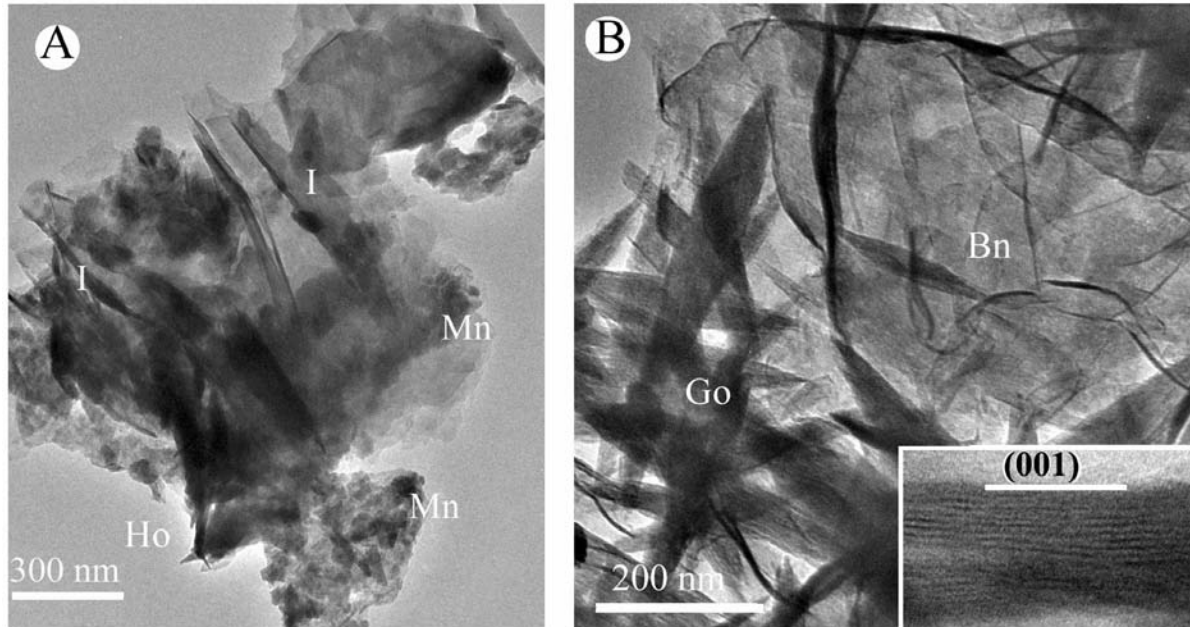
FIGURE 3. Bright-field TEM images showing aggregates of very thin birnessite plates in the dendrite sample UNM-M-1054 (**a**) and coexisting sheet-like birnessite and spindle-shaped goethite crystals in the second dendrite (**b**). Inserted in **b** is a HRTEM image showing ~7 Å (001) lattice fringes of birnessite. I = illite; Ho = hollandite; Mn = Mn-oxide aggregate; Go = goethite; Bn = birnessite.

FIGURE 4. TEM images of trilling todorokite in the sample AV1. (**a**) Low magnification of trilling intergrowth of todorokite fibers. (**b**) Aggregation of platy todorokite crystals. Individual plates have a morphology similar to that of birnessite. (**c**) Trilling todorokite crystals have many octahedral chain-width errors (see HRTEM images in Fig. 6 for details). (**d**) SAED pattern of trilling todorokite showing weak streaking diffractions along $a*$ directions.
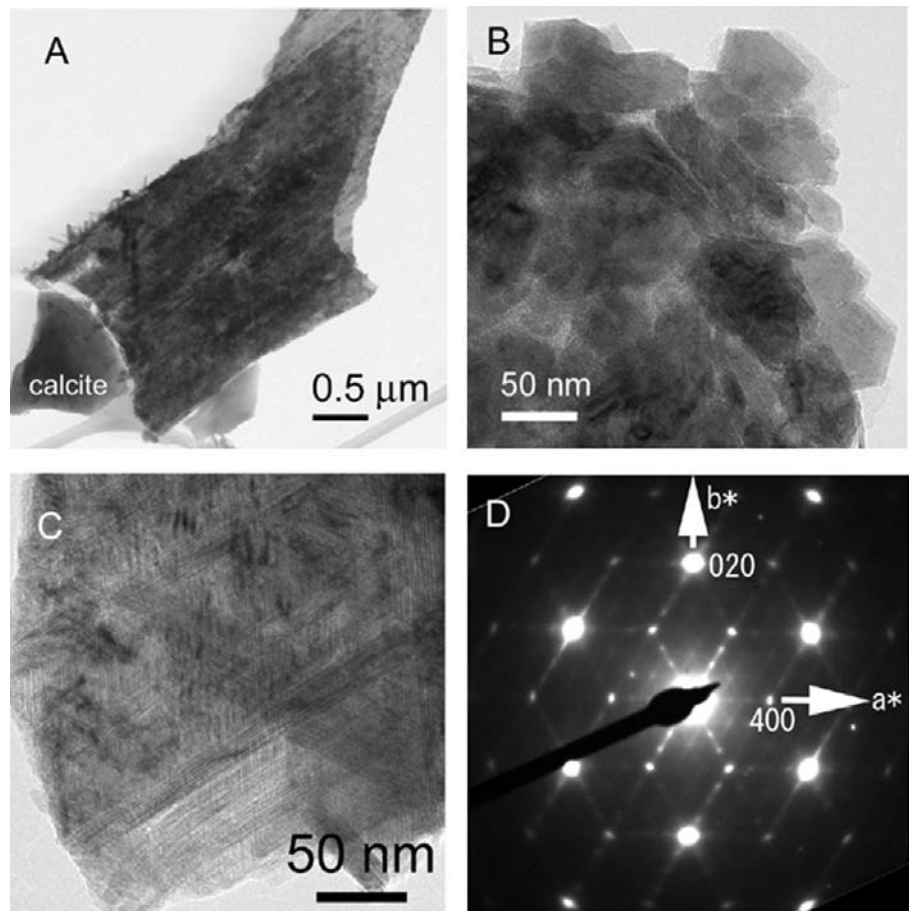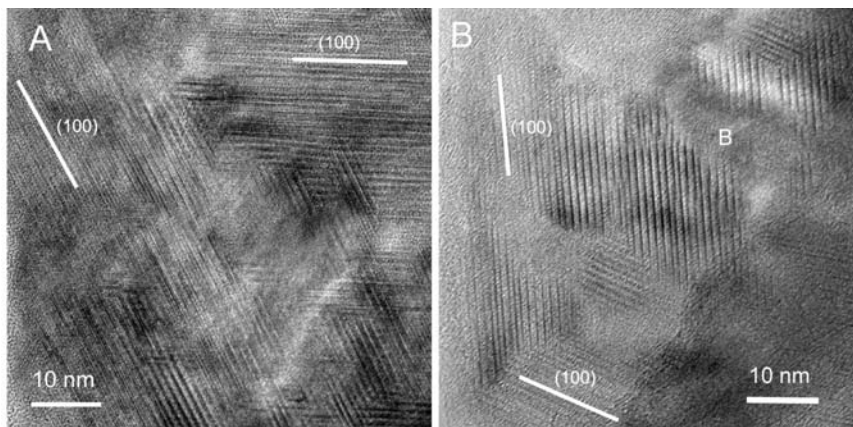
FIGURE 5. HRTEM images of trilling todorokite from Altmühl Valley, Germany. (**a**) HRTEM image of Figure 4c. Because each individual todorokite crystal is very thin, the overlap of lattice fringes from individual crystals result in the trilling pattern of lattice fringes. (**b**) HRTEM image of Figure 4b. The area "B" indicates a birnessite domain without any "superlattice" fringes from todorokite. Todorokite crystals are intergrown with birnessite. Intergrowth planes of trilling todorokite crystals are along {*hk*0}.
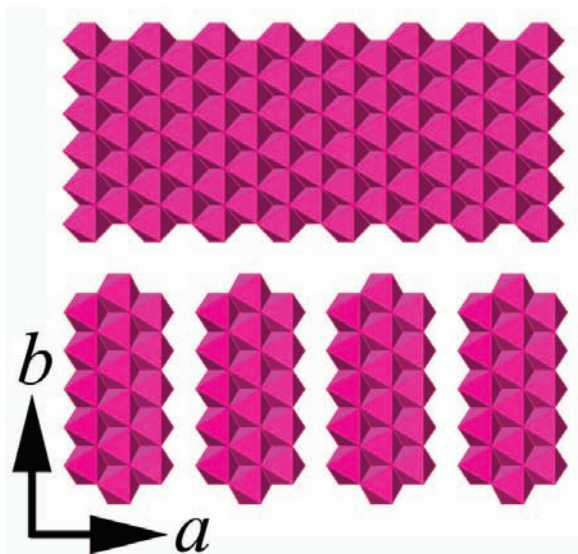
FIGURE 6. Polyhedral drawings of birnessite octahedral sheet (top) and todorokite octahedral triple chains (bottom). Todorokite octahedral wall layer parallel to (001) is derived from birnessite octahedral sheet by removing a single octahedral layer. *a* and *b* indicate directions of crystallographic axes for todorokite.
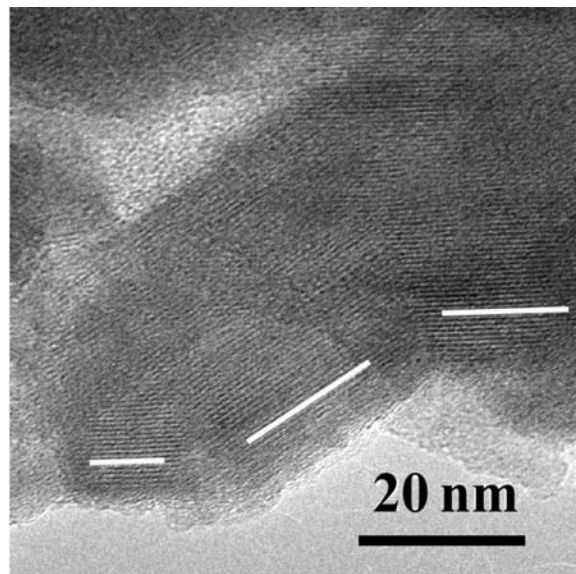

FIGURE 7. (**a**) HRTEM image of the T(2, 2) hollandite nanocrystals related by 120° rotation from Altmühl Valley, Germany. The white lines indicate the direction of octahedral chains.

2004), or hydrothermal treatment of buserite (Ching et al. 1999). The resulting todorokite crystals have a fibrous shape and show a trilling intergrowth. Based on overall hexagonal morphology and chain-width disorder the todorokite with trilling intergrowth could be transformed from its precursor birnessite.

One alternative explanation is that the todorokite intergrowths with (001) intergrowth planes may also form by epitaxial growth rather than the rearrangement of birnessite sheet layers. An octahedral wall layer of todorokite is an alternation of triple octahedral chains with an empty space equivalent to a single octahedral chain, and can be considered part of a birnessite octahedral sheet (Fig. 6). Todorokite grows epitaxially on the octahedral layer. Because the birnessite octahedral sheet has a pseudo-hexagonal symmetry, todorokite has three orientations against the substrate todorokite, i.e., trilling intergrowth.

The idealized structures of some manganese oxide minerals with tunnel and sheet structures can be described using a modular structure model (Turner and Buseck 1981). The width of tunnel can be expressed as number of octahedra. For instance, the tunnel structure in hollandite has a width of two octahedra on each side, and a notation of T(2, 2) is assigned for hollandite. Birnessite has a sheet structure or ∞ numbers of octahedra.
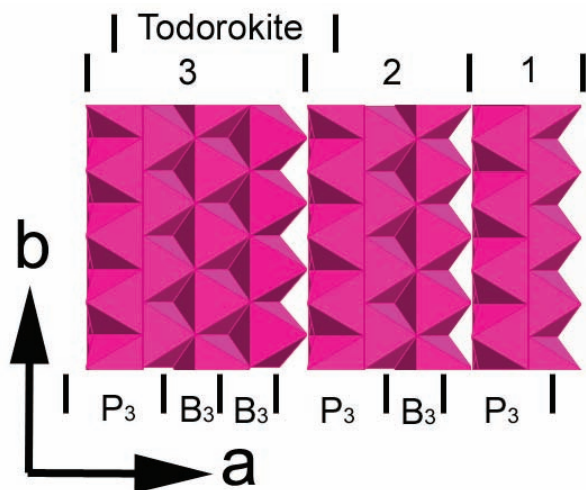
FIGURE 8. Polysomatic series of triple octahedral chain (todorokite), double octahedral chain, and single octahedral chain [pyrolusite analog with a (010) triple chain octahedral wall] structures (Veblen 1991). The numbers 1, 2, and 3 denote single, double, and triple octahedral chains, respectively. P_3 indicates a polysome of T(3, 1) pyrolusite analog, whereas B_3 indicates a polysome of T(3, ∞) 10 Å birnessite structure.

A todorokite structure with 3×3 octahedral tunnels can be divided into a polysome of pyrolusite-like structure (P_3) with 1-octahedral × 3-octahedral tunnels and two polysomes of an expanded birnessite-like structure (B_3), which is $\infty \times 3$ (Veblen 1991). A combination of these polysomes can describe a variety of chain width errors in todorokite (Fig. 8). A double manganese octahedral chain structure T(2, 3) is described as $P_3 B_3$, whereas a triple manganese octahedral chain structure (todorokite) T(3, 3) is described as $P_3 B_3 B_3$. The subscript number refers to the number of octahedral chains parallel to the octahedral wall parallel to (100) (Veblen 1991).

Chain-width disorder and chain termination in pyriboles can indicate solid-state reaction mechanism (Veblen 1981; Veblen and Buseck 1980). A similar phenomenon also occurs in the todorokite (Fig. 9). A termination rule for cooperative termination of octahedral chains in manganese minerals is derived from the geometry of octahedral chains and the octahedral wall layer. The tunnels with n chains are sandwiched by two octahedral wall layers in the T(n, 3) octahedral chain structure. Therefore, the dimension of a unit of T(n, 3) octahedral chain structure is an n+1 multiple of the single octahedral chain width (~0.23 nm), whereas the approximate tunnel dimension of a T(n, 3) octahedral structure is ideally 3n octahedral chain widths. Figure 9 shows examples of octahedral chain terminations. For structural coherence at a termination, the sum of the numbers of octahedral wall layers and octahedral chains must be equal at both sides beyond the termination. Frequent occurrence of octahedral chain terminations suggests that the todorokite was derived from birnessite structure or multiple todorokite nucleations occurred on octahedral wall layer of todorokite.

Precipitation of manganese oxides in natural environments can be resulted from microbial processes (Tebo et al. 1997, 2004, 2005). Microbes accelerate the rate of Mn^{2+} oxidation by up to
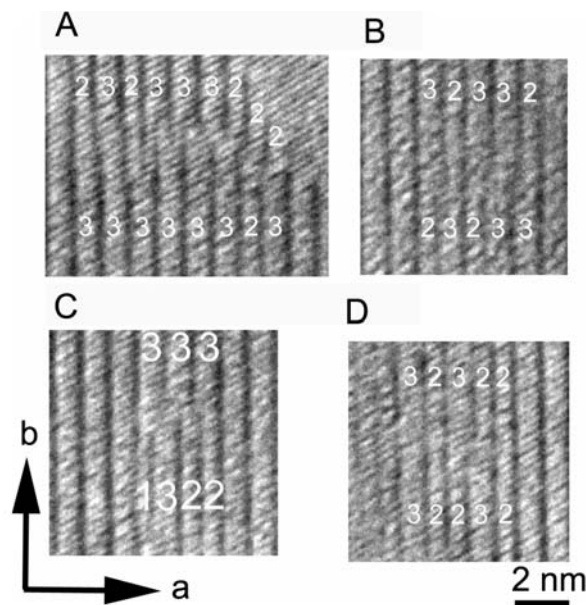
FIGURE 9. HRTEM images of coherent zipper terminations in todorokite structure from Altmühl Valley, Germany. The a^* axis is horizontal and the b^* axis is vertical. (**a**) The octahedral chain sequence (23233322) changes to (33333323). Birnessite appears at the upper right corner of the image. (**b**) The chain sequence (323332) changes to (23233). (**c**) The chain sequence (333) changes to (1322). (**d**) The chain sequence (32322) changes to (32232).

five orders of magnitude compared to abiotic Mn^{2+} oxidation (Tebo et al. 1997). Although details of the transformation from buserite to todorokite are not clear, the availability of Mn^{3+} affects the transformation (Cui et al. 2008). Mn^{3+} is unstable in wet environment (Cui et al. 2008). Therefore, the oxidation process of some Mn^{2+} or Mn^{3+} are required to form todorokite. Future study on the role of microbes in the dendrite formation may be able to address this problem.

REFERENCES CITED

Bodei, S., Manceau, A., Geoffroy, N., Baronnet, A., and Buatier, M. (2007) Formation of todorokite from vernadite in Ni-rich hemipelagic sediments. Geochimica et Cosmochimica Acta, 71, 5698–5716.

Ching, S., Krukowska, K.S., and Suib, S.L. (1999) A new synthetic route to todorokite-type manganese oxides. Inorganica Chimica Acta, 294, 123–132.

Chopard, B., Herrmann, H.J., and Vicsek, T. (1991) Structure and growth mechanism of mineral dendrites. Nature, 353, 409–412.

Cui, H., Liu, X., Tan, W., Feng, X., Liu, F., and Huada, D.R. (2008) Influence of Mn(III) availability on the phase transformation from layered buserite to tunnel-structured todorokite. Clays and Clay Minerals, 56, 397–403.

Feng, Q., Kanoh, H., Miyai, Y., and Ooi, K. (1995) Metal-ion extraction/insertion reactions with todorokite-type manganese oxide in the aqueous-phase. Chemistry of Material, 7, 1722–1727.

Feng, X.H., Tan, W.F., Liu, F., Wang, J.B., and Ruan, H.D. (2004) Synthesis of todorokite at atmospheric pressure. Chemistry of Materials, 16, 4330–4336.

Golden, D.C., Chen, C.C., and Dixon, J.B. (1986) Synthesis of todorokite. Science,

231, 717–719.

——— (1987) Transformation of birnessite to buserite, todorokite, and manganite under mild hydrothermal treatment. Clays and Clay Minerals, 35, 271–280.

Hiemenz, P.C. and Rajagopalan, R. (1997) Principles of Colloid and Surface Chemistry, 672 p. Marcel Dekker, New York.

Klein, C. (2002) Manual of Mineral Science, 641 p. Wiley, New York.

Krinsley, D. (1998) Models of rock varnish formation constrained by high resolution transmission electron microscopy. Sedimentology, 45, 711–725.

Krinsley, D., Dorn, R., and Tovey, N.K. (1995) Nanometer-scale layering in rock varnish: Implications for genesis and paleoenvironmental interpretation. Journal of Geology, 103, 106–113.

McKeown, D.A. and Post, J.E. (2001) Characterization of manganese oxide mineralogy in rock varnish and dendrites using X-ray absorption spectroscopy. American Mineralogist, 86, 701–713.

Nagy, B., Nagy, L.A., Rigali, M.J., Jones, W.D., Krinsley, D.H., and Sinclair, N.A. (1991) Rock varnish in the Sonoran Desert: Microbiologically mediated accumulation of manganiferous sediments. Sedimentology, 38, 1153–1171.

Palmer, F.E., Staley, J.T., Murray, R.G.E., Counsell, T., and Adams, J.B. (1986) Identification of manganese-oxidizing bacteria from desert varnish. Geomicrobiology Journal, 4, 343–360.

Perry, R.S. and Adams, J.B. (1978) Desert varnish: Evidence for cyclic deposition of manganese. Nature, 276, 489–491.

Post, J.E. (1999) Manganese oxide minerals: Crystal structures and economic and environmental significance. Proceedings of the National Academy of Sciences of the United States of America, 96, 3447–3454.

Potter, R.M. and Rossman, G.R. (1977) Desert varnish: The importance of clay minerals. Science, 196, 1446–1448.

——— (1979) Mineralogy of manganese dendrites and coatings. American Mineralogist, 64, 1219–1226.

Siegel, M.D. and Turner, S. (1983) Crystalline todorokite associated with biogenic debris in manganese nodules. Science, 219, 172–174.

Tebo, B.M., Ghiorse, W.C., vanWaasbergen, L.G., Siering, P.L., and Caspi, R. (1997) Bacterially mediated mineral formation: Insights into manganese(II) oxidation from molecular genetic and biochemical studies. In J.E. Banfield and K.H. Nealson, Eds., Geomicrobiology: Interactions between microbes and minerals, 35, p. 225–266. Reviews in Mineralogy and Geochemistry, Mineralogical Society of America, Chantilly, Virginia.

Tebo, B.M., Bargar, J.R., Clement, B.G., Dick, G.J., Murray, K.J., Parker, D., Verity, R., and Webb, S.M. (2004) Biogenic manganese oxides: Properties and mechanisms of formation. Annual Review of Earth and Planetary Sciences, 32, 287–328.

Tebo, B.M., Johnson, H.A., McCarthy, J.K., and Templeton, A.S. (2005) Geomicrobiology of manganese(II) oxidation. Trends in Microbiology, 13, 421–428.

Tsuji, M. and Komarneni, S. (1993) Selective exchange of divalent transition-metal ions in cryptomelane-type manganic acid with tunnel structure. Journal of Materials Research, 8, 611–616.

Turner, S. and Buseck, P.R. (1981) Todorokites: A new family of naturally occurring manganese oxides. Science, 212, 1024–1027.

Veblen, D.R. (1981) Non-classical pyriboles and polysomatic reactions in biopyriboles. In D.R. Veblen, Ed., Amphiboles and Other Hydrous Pyriboles—Mineralogy, 9A, p. 189–236. Reviews in Mineralogy and Geochemistry, Mineralogical Society of America, Chantilly, Virginia.

——— (1991) Polysomatism and polysomatic series: A review and applications. American Mineralogist, 76, 801–826.

Veblen, D.R. and Buseck, P.R. (1980) Microstructures and reaction mechanisms in biopyriboles. American Mineralogist, 65, 599–623.

Wenk, H.R. and Bulakh, A. (2004) Minerals: Their constitution and origin, 668 p. Cambridge University Press, New York.

Xu, H.F. and Wang, Y. (2000) Crystallization sequence and microstructure evolution of Synroc samples crystallized from $CaZrTi_2O_7$ melts. Journal of Nuclear Materials, 279, 100–106.